Research Article | Vol. 25, No. 11 | 29 May 2017 | OPTICS EXPRESS 12381
Optics EXPRESS

Monolithic CMOS-compatible zero-index metamaterials

Daryl I. Vulis,[1,5] Yang Li,[1,5,*] Orad Reshef,[1,2,5] Philip Camayd-Muñoz,[1] Mei Yin,[1,3] Shota Kita,[1,4] Marko Lončar,[1] and Eric Mazur[1]

[1]*Department of Physics and School of Engineering and Applied Sciences, Harvard University, 9 Oxford Street, Cambridge, MA 02138, USA*
[2]*Current address: Department of Physics, University of Ottawa, 25 Templeton Street, Ottawa, Ontario K1N 6N5, Canada*
[3]*Current address: Network Department, China Mobile Communications Corporation, 29 Financial Street, Beijing 100033, China*
[4]*Current address: Photonic Nano-Structure Research Group, Optical Science Laboratory, NTT Basic Research Laboratory, 3-1 Wakamiya, Morinosato, Atsugi, Kanagawa 243-0198, Japan*
[5]*These authors contributed equally to this work.*
[*]*yli@seas.harvard.edu*

Abstract: Zero-index materials exhibit exotic optical properties that can be utilized for integrated-optics applications. However, practical implementation requires compatibility with complementary metallic-oxide-semiconductor (CMOS) technologies. We demonstrate a CMOS-compatible zero-index metamaterial consisting of a square array of air holes in a 220-nm-thick silicon-on-insulator (SOI) wafer. This design supports zero-index modes with Dirac-cone dispersion. The metamaterial is entirely composed of silicon and offers compatibility through low-aspect-ratio structures that can be simply fabricated in a standard device layer. This platform enables mass adoption and exploration of zero-index-based photonic devices at low cost and high fidelity.

OCIS codes: (130.0130) Integrated optics; (160.3918) Metamaterials; (220.4241) Nanostructure fabrication; (230.0230) Optical devices.

References and links

1. R. Soref, "The past, present, and future of silicon photonics," IEEE J. Sel. Top. Quantum Electron. **12**, 1678–1687 (2006).
2. B. Jalali and S. Fathpour, "Silicon photonics," J. Lightwave Technol. **24**, 4600–4615 (2006).
3. M. Lipson, "Guiding, modulating, and emitting light on silicon-challenges and opportunities," J. Lightwave Technol. **23**, 4222–4238 (2005).
4. D. A. B. Miller, "Device requirements for optical interconnects to silicon chips," Proc. IEEE **97**, 1166–1185 (2009).
5. N. Engheta, "Pursuing near-zero response," Science **340**, 286–287 (2013).
6. X. Huang, Y. Lai, Z. H. Hang, H. Zheng, and C. T. Chan, "Dirac cones induced by accidental degeneracy in photonic crystals and zero-refractive-index materials," Nat. Mater. **10**, 582–586 (2011).
7. P. Moitra, Y. Yang, Z. Anderson, I. I. Kravchenko, D. P. Briggs, and J. Valentine, "Realization of an all-dielectric zero-index optical metamaterial," Nat. Photonics **7**, 791–795 (2013).
8. R. Maas, J. Parsons, N. Engheta, and A. Polman, "Experimental realization of an epsilon-near-zero metamaterial at visible wavelengths," Nat. Photonics **7**, 907–912 (2013).
9. S. Kocaman, M. S. Aras, P. Hsieh, J. F. McMillan, C. G. Biris, N. C. Panoiu, M. B. Yu, D. L. Kwong, A. Stein, and C. W. Wong, "Zero phase delay in negative-refractive-index photonic crystal superlattices," Nat. Photonics **5**, 499–505 (2011).
10. K. Sakoda, "Dirac cone in two- and three-dimensional metamaterials," Opt. Express **20**, 3898–3917 (2012).
11. J. Schilling, "Fundamental optical physics: The quest for zero refractive index," Nat. Photonics **5**, 449–451 (2011).
12. I. Liberal and N. Engheta, "Zero-index platforms: Where light defies geometry," Optics & Photonics News **27**, 26–33 (2016).
13. I. Liberal and N. Engheta, "Near-zero refractive index photonics," Nat. Photonics **11**, 149–158 (2017).
14. M. Z. Alam, I. De Leon, and R. W. Boyd, "Large optical nonlinearity of indium tin oxide in its epsilon-near-zero region," Science **352**, 795–797 (2016).
15. N. M. Litchinitser, A. I. Maimistov, I. R. Gabitov, R. Z. Sagdeev, and V. M. Shalaev, "Metamaterials: electromagnetic enhancement at zero-index transition," Opt. Lett. **33**, 2350–2352 (2008).

#281211 https://doi.org/10.1364/OE.25.012381
Journal © 2017 Received 23 Nov 2016; accepted 20 Apr 2017; published 18 May 2017

Optics EXPRESS

16. L. Caspani, R. P. M. Kaipurath, M. Clerici, M. Ferrera, T. Roger, J. Kim, N. Kinsey, M. Pietrzyk, A. Di Falco, V. M. Shalaev, A. Boltasseva, and D. Faccio, "Enhanced nonlinear refractive index in ϵ-Near-Zero materials," Phys. Rev. Lett. **116**, 233901 (2016).
17. D. de Ceglia, S. Campione, M. A. Vincenti, F. Capolino, and M. Scalora, "Low-damping epsilon-near-zero slabs: Nonlinear and nonlocal optical properties," Phys. Rev. B Condens. Matter **87**, 155140 (2013).
18. C. Argyropoulos, G. D'Aguanno, and A. Alù, "Giant second-harmonic generation efficiency and ideal phase matching with a double ϵ-near-zero cross-slit metamaterial," Phys. Rev. B Condens. Matter **89**, 235401 (2014).
19. M. G. Silveirinha and N. Engheta, "Theory of supercoupling, squeezing wave energy, and field confinement in narrow channels and tight bends using ϵ near-zero metamaterials," Phys. Rev. B Condens. Matter **76**, 1–17 (2007).
20. M. Silveirinha and N. Engheta, "Tunneling of electromagnetic energy through subwavelength channels and bends using epsilon-near-zero materials," Phys. Rev. Lett. **97**, 157403 (2006).
21. A. M. Mahmoud, I. Liberal, and N. Engheta, "Dipole-dipole interactions mediated by epsilon-and-mu-near-zero waveguide supercoupling [invited]," Opt. Mater. Express **7**, 415–424 (2017).
22. Y. Zhou, X.-T. He, F.-L. Zhao, and J.-W. Dong, "Proposal for achieving in-plane magnetic mirrors by silicon photonic crystals," Opt. Lett. **41**, 2209–2212 (2016).
23. H. Hajian, E. Ozbay, and H. Caglayan, "Enhanced transmission and beaming via a zero-index photonic crystal," Appl. Phys. Lett. **109**, 031105 (2016).
24. J. Hao, W. Yan, and M. Qiu, "Super-reflection and cloaking based on zero index metamaterial," Appl. Phys. Lett. **96**, 101109 (2010).
25. V. C. Nguyen, L. Chen, and K. Halterman, "Total transmission and total reflection by zero index metamaterials with defects," Phys. Rev. Lett. **105**, 233908 (2010).
26. M. Memarian and G. V. Eleftheriades, "Dirac leaky-wave antennas for continuous beam scanning from photonic crystals," Nat. Commun. **6**, 5855 (2015).
27. R. Sokhoyan and H. A. Atwater, "Quantum optical properties of a dipole emitter coupled to an ϵ-near-zero nanoscale waveguide," Opt. Express **21**, 32279–32290 (2013).
28. A. Alù and N. Engheta, "Boosting molecular fluorescence with a plasmonic nanolauncher," Phys. Rev. Lett. **103**, 043902 (2009).
29. I. Liberal and N. Engheta, "Zero-index structures as an alternative platform for quantum optics," Proc. Natl. Acad. Sci. U. S. A. **114**, 822–827 (2017).
30. H. Suchowski, K. O'Brien, Z. J. Wong, A. Salandrino, X. Yin, and X. Zhang, "Phase mismatch–free nonlinear propagation in optical zero-index materials," Science **342**, 1223–1226 (2013).
31. O. Reshef, Y. Li, M. Yin, L. Christakis, D. I. Vulis, P. Muñoz, S. Kita, M. Loncar, and E. Mazur, "Phase-matching in dirac-cone-based zero-index metamaterials," in Conference on Lasers and Electro-Optics (Optical Society of America, 2016), paper JTu5A.53 .
32. A. Boltasseva and H. A. Atwater, "Low-loss plasmonic metamaterials," Science **331**, 290–291 (2011).
33. Y. Li, S. Kita, P. Muñoz, O. Reshef, D. I. Vulis, M. Yin, M. Lončar, and E. Mazur, "On-chip zero-index metamaterials," Nat. Photonics **9**, 738–742 (2015).
34. S. Kita, Y. Li, P. Camayd-Muñoz, O. Reshef, D. I. Vulis, R. W. Day, E. Mazur, and M. Lončar, "On-chip all-dielectric fabrication-tolerant zero-index metamaterials," Opt. Express **25**, 8326–8334 (2017).
35. X.-T. He, Z.-Z. Huang, M.-L. Chang, S.-Z. Xu, F.-L. Zhao, S.-Z. Deng, J.-C. She, and J.-W. Dong, "Realization of zero-refractive-index lens with ultralow spherical aberration," ACS Photonics **3**, 2262–2267 (2016).
36. J. D. Joannopoulos, S. G. Johnson, J. N. Winn, and R. D. Meade, *Photonic Crystals: Molding the Flow of Light* (Princeton University Press, 2011).
37. A. Yariv, *Optical Electronics in Modern Communications* (Oxford University Press, 1997).
38. K. Sakoda, "Proof of the universality of mode symmetries in creating photonic dirac cones," Opt. Express **20**, 25181–25194 (2012).
39. B. Zhen, C. W. Hsu, Y. Igarashi, L. Lu, I. Kaminer, A. Pick, S.-L. Chua, J. D. Joannopoulos, and M. Soljačić, "Spawning rings of exceptional points out of dirac cones," Nature **525**, 354–358 (2015).
40. S. Nagai and A. Sanada, "Γ-point group velocity of lossy dirac cone composite right/left-handed metamaterials," IEICE Electronics Express **13**, 20160281–20160281 (2016).
41. M. Faryad and M. W. Ashraf, "On the mapping of dirac-like cone dispersion in dielectric photonic crystals to an effective zero-index medium," J. Opt. Soc. Am. B **33**, 1008–1013 (2016).
42. C. W. Hsu, B. Zhen, A. Douglas Stone, J. D. Joannopoulos, and M. Soljačić, "Bound states in the continuum," Nature Reviews Materials **1**, 16048 (2016).
43. P. Muñoz, S. Kita, O. Mello, O. Reshef, D. I. Vulis, Y. Li, M. Loncar, and E. Mazur, "Lossless integrated dirac-cone metamaterials," in Conference on Lasers and Electro-Optics (Optical Society of America, 2016), paper JW2A.24 .
44. C. R. Simovski and S. A. Tretyakov, "Local constitutive parameters of metamaterials from an effective-medium perspective," Phys. Rev. B Condens. Matter **75**, 195111 (2007).
45. D. R. Smith, D. C. Vier, T. Koschny, and C. M. Soukoulis, "Electromagnetic parameter retrieval from inhomogeneous metamaterials," Phys. Rev. E **71**, 1–11 (2005).
46. R. A. Shore and A. D. Yaghjian, "Traveling waves on two- and three-dimensional periodic arrays of lossless scatterers," Radio Sci. **42**, RS6S21 (2007).
47. A. Alù, A. D. Yaghjian, R. A. Shore, and M. G. Silveirinha, "Causality relations in the homogenization of

Optics EXPRESS

metamaterials," Phys. Rev. B Condens. Matter **84**, 054305 (2011).

1. Introduction

Silicon photonics has become the principal platform for on-chip optical telecommunications [1–3]. Furthermore, monolithic fabrication of many silicon-based photonic devices allows for integration with existing CMOS technologies that currently dominate computation and communications [3,4]. As integrated silicon photonics approaches the nanoscale, solutions based on new materials are necessary to manage the confinement and behavior of light. Metamaterials offer a way to engineer materials with novel, tailored properties that extend the capabilities of silicon photonics.

Zero-refractive-index metamaterials have attracted attention for engineering the interaction of light in integrated photonics [5–13]. The effective wavelength within this material is infinite, allowing phase-free propagation of light as well as strong nonlinear optical enhancement [14–18]. Such extreme properties have inspired a variety of applications, including efficient coupling between disparate modes and sub-diffraction limit waveguide design [8, 19–23], electromagnetic cloaking [24, 25], beam steering [26], quantum optics [27–29], and new approaches to phase matching in nonlinear optics [18, 30, 31].

Effective implementation of a zero-refractive-index metamaterial in integrated photonics requires both CMOS compatibility and monolithic fabrication: the zero-index metamaterial must 1) be fully dielectric, 2) contain low-aspect-ratio structures for compatibility with standard SOI wafers, and 3) operate at telecom frequencies. Integrated applications also necessitate an in-plane geometry in which light propagates parallel to the substrate surface for compatibility with silicon waveguides or photonic devices.

Inspection of the definition of refractive index ($n_r^{eff} = \sqrt{\epsilon_r^{eff}\mu_r^{eff}}$) reveals that an index of zero is achieved if either or both the electric (ϵ_r^{eff}) or magnetic (μ_r^{eff}) response of a material is tuned to zero. While we can tune the electric and magnetic response using metallic inclusions [8, 32], incorporating metals results in Ohmic losses and incompatibility with all-dielectric silicon photonics. In addition, inspection of the impedance equation ($Z_r^{eff} = \sqrt{\mu_r^{eff}/\epsilon_r^{eff}}$) reveals that this "single zero" case produces an impedance of either infinity or zero – a mismatch that makes such metamaterials unsuitable for integrated applications. Fully dielectric zero-index metamaterials present an attractive alternative. Such metamaterials can be achieved by tuning Mie resonances in a photonic crystal structure [6, 10]. This approach allows for precise and independent control of the electric and magnetic response and can be used to tune both the effective relative permittivity ϵ_r^{eff} and effective relative permeability μ_r^{eff} to zero simultaneously, yielding a finite impedance [6].

Previous all-dielectric zero-index metamaterial designs are largely unsuitable for integrated photonic applications. For example, out-of-plane configurations in which light propagates perpendicular to the substrate surface are impractical for integrated applications or long interaction lengths [7]. In comparison, in-plane configurations formed by cascading regions of both negative and positive phase advance do not offer flexible shape configuration or isotropic behavior [9]. Finally, zero-refractive-index metamaterials have been demonstrated by our group for an in-plane configuration with isotropic behavior. However, these metamaterials rely on either a unit cell of artificially infinitely tall silicon pillars achieved through parallel conductors [33] or silicon pillars whose height considerably exceeds current standard SOI platforms [34].

Here, we present a monolithic, CMOS-compatible Dirac-cone metamaterial. Th3 metamaterial possesses a finite impedance and refractive index of zero for telecom frequencies. This metamaterial can be patterned and structured on a photonic chip in a single step alongside other optical elements, and is based on a standard material platform of 220-nm-thick SOI [Fig. 1].

The metamaterial design consists of a square array of air holes in 220-nm-thick SOI, which can be patterned using a single electron-beam-lithography procedure. The air holes are then structured through an inductively coupled plasma reactive ion etch procedure. To measure

Optics EXPRESS

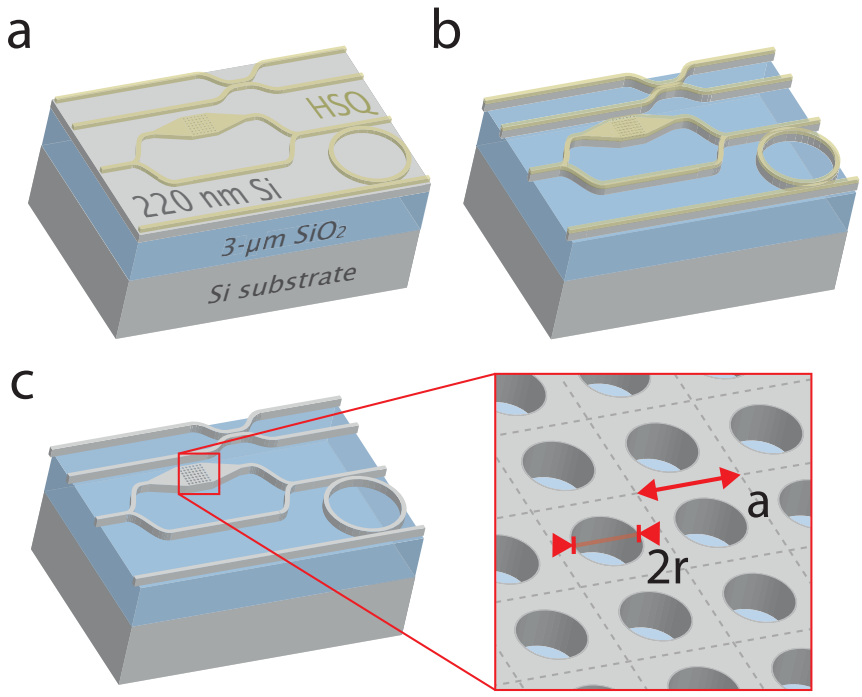

Fig. 1. Illustration of the fabrication stages of a sample photonic circuit that incorporates a zero-index metamaterial as a single, monolithic procedure. A substrate consisting of 220-nm-thick SOI is (a) patterned via electron beam lithography, then (b) structured through a reactive ion etch procedure, and finally (c) the resist is removed revealing the completed circuit. Inset: Close-up view of a metamaterial air-hole array with design parameters radius (r) and pitch (a) indicated.

the index of refraction, we construct a triangular prism of this metamaterial and observe that transverse-electric (TE) polarized light entering the prism is refracted perpendicular to the output facet through a semi-circular polymer waveguide. A zero degree angle of refraction, combined with a linear dispersion, unambiguously demonstrates a refractive index of zero.

Through configuration of the unit cells, the metamaterial can be defined in arbitrary shapes for varied potential applications. In addition, use of standard planar fabrication techniques maintains intrinsic compatibility with the vast library of existing SOI-based devices. This metamaterial enables the mass production of zero-index-based devices at low cost and high fidelity through CMOS fabrication techniques and possesses simple features consisting of nanoscale circular holes. Combined with a monolithic fabrication procedure, this platform provides an easily adaptable method of exploring various applications of a refractive index near zero.

2. Design and theory

To achieve a platform with low-aspect-ratio features, we increase the ratio of silicon to air as compared to previous zero-index designs based on infinitely tall silicon pillars [6, 7, 10, 33, 35]. An air hole in silicon matrix design increases the volume filling fraction of silicon, allowing the area between defined air columns to be used as short resonators suitable for thinner silicon films. The metamaterial is designed for TE polarized modes that are more strongly confined in thin silicon layers than transverse magnetic (TM) polarized modes [36, 37]. Furthermore, we

Optics EXPRESS

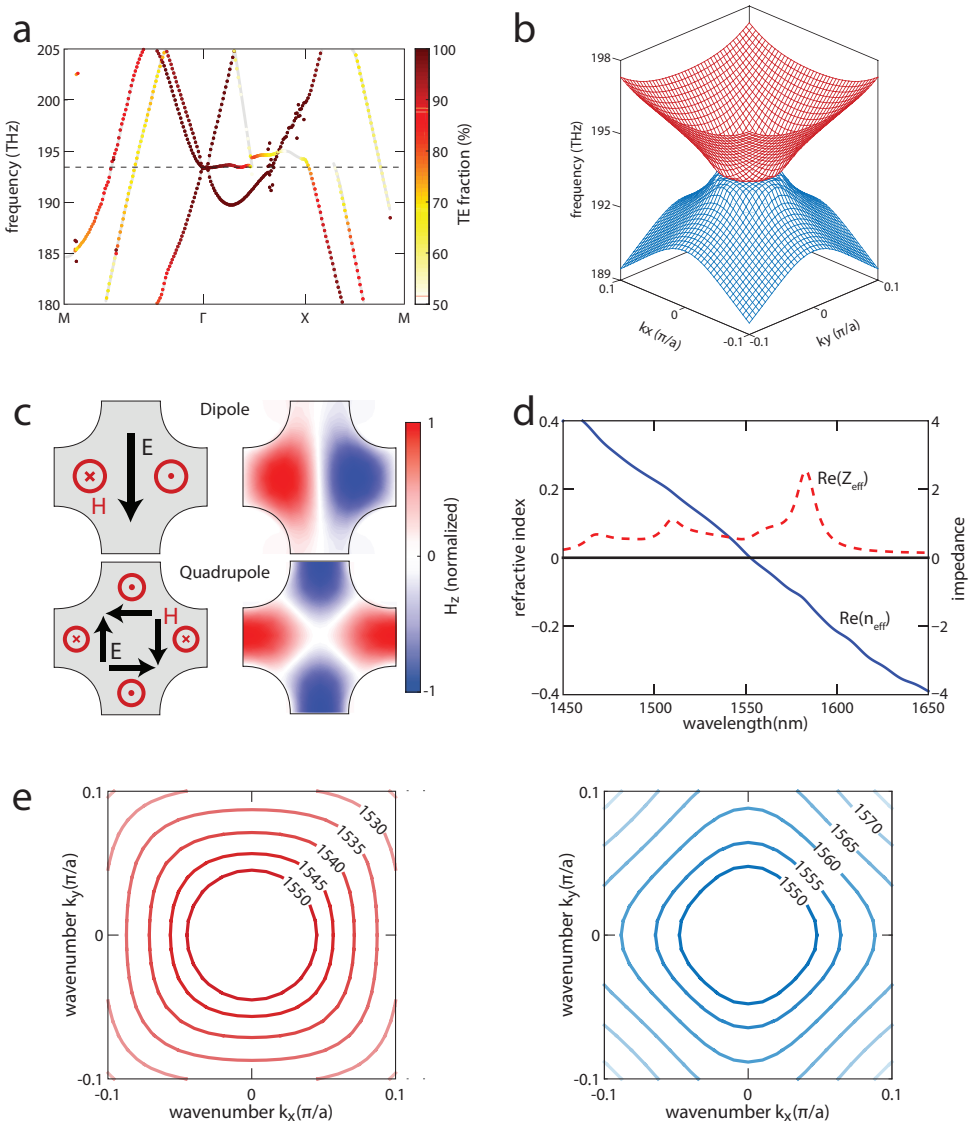

Fig. 2. Design of the zero-index metamaterial. (a) Photonic band structure of the zero-index metamaterial for TE modes. Two linear dispersion bands intersect at the Γ point at λ = 1550 nm. TE fraction is superimposed on the band structure. The grey lines are added to clarify the bands. (b) Three-dimensional dispersion surfaces. The linear bands (blue and red) form a Dirac-like cone. We show only the two modes that form the cone to clarify the dispersion. (c) Electric fields at the Γ point over a unit-cell cross section in the plane of the array, corresponding to an electric dipole mode and a magnetic quadrupole mode. (d) Effective index (blue line) and normalized impedance (red dashed line) of the metamaterial. The index crosses zero linearly at a wavelength of 1550 nm. Impedance is shown to have a finite value of 0.8 at the design wavelength. (e) Isowavelength contours of the zero-index metamaterial for wavelengths below (left) and above (right) the design wavelength. Lighter shades indicate wavelengths farther from the design wavelength. The nearly circular contours indicate that this metamaterial is almost isotropic near the Γ point.

Optics EXPRESS

expect symmetric modes to result from the symmetric unit cell lattice featured in an air-hole structure; such modes can form a degeneracy corresponding to a Dirac-cone dispersion [38]. We tune the size and separation of the air holes in our metamaterial to ensure the degeneracy of three symmetric modes at the Γ point and achieve a photonic Dirac cone at the center of the Brillouin zone [Fig. 2(a)] for a wavelength of 1550 nm. The pitch and radius are 738 nm and 222 nm, respectively.

The calculated band structure for the designed material is shown in Fig. 2(a). Two bands with linear dispersion intersect at the Γ point, forming a Dirac-like cone [6,10]. We also observe an additional "flat" band corresponding to a longitudinal electric dipole mode. The bands display quadratic-like dispersion in the vicinity of the Γ point, deviating from an ideal (linear) Dirac cone, with characteristics similar to previously observed rings of exceptional points [39]. The shape of this dispersion is more clearly observed in the three-dimensional dispersion surface shown in Fig. 2(b). For a sufficiently small exceptional ring diameter, we achieve degeneracy of the modes at the Γ point and expect behavior similar to that of a linear Dirac-cone dispersion.

The intersection of the two Dirac-cone bands corresponds to a degeneracy of electric dipole and magnetic quadrupole modes at the Γ point [Fig. 2(c)]. It should be emphasized that this degeneracy effectively produces a single hybridized mode [38] that oscillates between dipole and quadrupole symmetries; as such this hybridized mode can support a propagating wave with real power flow identical to those found in other Dirac cone zero-index metamaterials [6, 7, 33] (See Appendix A5).

In addition, we observe a disparity between the quality factors of the two degenerate modes that produces a quadratic dispersion in the vicinity of the Γ point. The quality factor of the dipole and quadrupole modes are estimated to be 40 and 5500, respectively. Radiative loss produced by the dipole mode disrupts the degenerate behavior and results in a lower group velocity near the Γ point, producing the quadratic bands in that region [39, 40]. Conversely, the quadrupole modes do not produce significant radiation losses as there is a symmetry mismatch of that mode in relation to plane waves [Fig. 2(c)].

While Dirac-cone behavior as the product of dipole and quadrupole modes has been predicted [26, 38, 39], treatment of a material with a Dirac-cone dispersion comprised of these modes as an effectively zero-index medium may be challenging [41]. This work represents the first demonstration of zero-index via degeneracy involving a quadrupole mode. Consideration of homogenization criteria ensures that the modes excited in the presented metamaterial by a normal incidence plane-wave source produce an effectively zero-index (See Appendix A4 for homogenization verification).

Despite the low-aspect ratio, this metamaterial maintains propagation losses that are comparable to previously demonstrated zero-index metamaterials. Low confinement and the resulting propagation loss is intrinsic to modes that reside at the Γ point and above the light line. As such, it cannot be trivially confined to the plane of propagation. However, through removal of the metallic mirrors present in our earlier work [33] there is the possibility of complete elimination of out-of-plane radiation loss through the use of a single all-dielectric CMOS-compatible distributed Bragg reflector. Addition of such a reflector allows for the formation of a bound state in the continuum [42]. There have been some initial efforts towards achieving this goal [43] that are beyond the scope of this manuscript (See Appendix A2 for propagation losses).

The TE fraction $(1 - \int |\overrightarrow{E_z}|^2 dV / \int |\overrightarrow{E}|^2 dV)$ of the modes is superimposed on the band structure in Fig. 2(a); high TE polarization fraction in the modes forming the Dirac cone indicates that TE polarized light entering the structure efficiently couples to modes forming the degeneracy. While there are multiple modes at most frequencies, including the zero-index frequency, systematic analysis of these modes reveal that those beyond the Dirac cone possess either a low TE polarization fraction or modal symmetry that is incompatible with a plane wave source; as such they are unlikely to be accessed by the TE plane wave source (See Appendix A4 for

Optics EXPRESS

homogenization verification).

We extract the effective refractive index and impedance of the metamaterial by simulating the scattering parameters of a finite metamaterial slab [Fig. 2(d)] [44] (See Appendix A1). We find that the refractive index crosses zero with linear dispersion in the vicinity of the Dirac cone at the design wavelength of 1550 nm. We also observe that the material has an effective normalized impedance of 0.8 at that design wavelength. From the surface in Fig. 2(b) and the collapsed isowavelength contours corresponding to frequencies above and below the design wavelength in Fig. 2(e), we observe that the modes at the Γ point form nearly circular isowavelength contours close to the design wavelength, indicating isotropic behavior (See Appendix A4 for homogenization verification and isowavelength contour fitting).

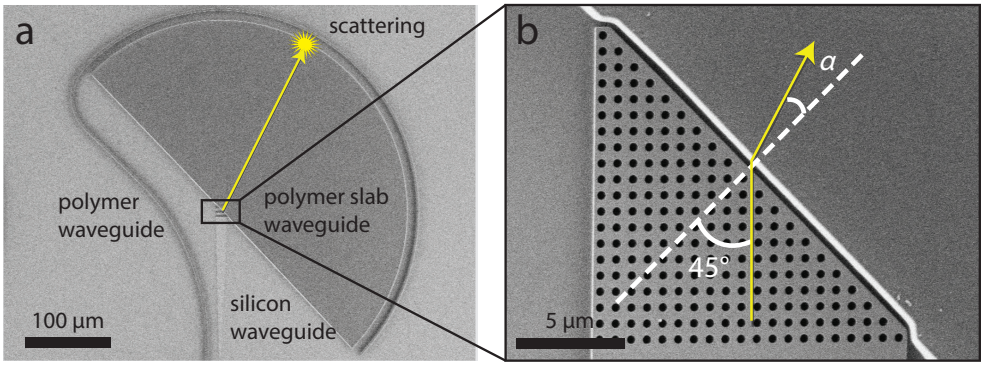

Fig. 3. Fabricated metamaterial and experimental setup. (a) Scanning electron microscopy image of the fabricated device. A silicon waveguide carries the incident beam towards the zero-index metamaterial prism as outlined in black, where the beam is refracted into the SU-8 slab waveguide. A silicon lip at the outside edge of the slab waveguide is used to scatter the output beam for optimal imaging. The angle of refraction α is determined by measuring the position of the refracted beam at the curved output edge of polymer slab waveguide as indicated by the yellow scattering point. An additional polymer waveguide around the outside edge of the slab waveguide includes defects that are used to align the infrared images during experimental data processing. (b) Fabricated zero-index metamaterial prism showing the incident and refracted beams

3. Experimental results

To experimentally measure the refractive index, we constructed a right triangular prism of this metamaterial and measured the refraction of TE polarized light entering the prism. Fig. 3 shows a scanning electron microscope image of the fabricated device, including input and output coupling structures [Fig. 3(a)] and a close-up image of the fabricated metamaterial prism [Fig. 3(b)]. TE polarized light is coupled into the metamaterial through a tapered silicon waveguide. This ensures plane-wave excitation of the modes corresponding to a refractive index of zero. Light exits the prism via the output facet into a semicircular polymer (SU-8) slab waveguide. The exiting light propagates radially outward to the edge of the slab waveguide [Fig. 3(a)]. To extract the angle of refraction, α, the scattered beam is imaged by a near-infrared camera [Fig. 3(b)].

We measure the angle of refraction of the metamaterial by sampling the intensity at the outer edge of the SU-8 slab waveguide for each of the wavelengths ranging from 1480 nm through 1680 nm [Fig. 4(a)]. The data show a clear linear transition from a positive-index regime to a negative-index regime, crossing zero at a wavelength of 1625 nm. We also observe an additional, weaker beam at +45°. We attribute this additional beam to TM modes in the metamaterial, as we

Optics EXPRESS

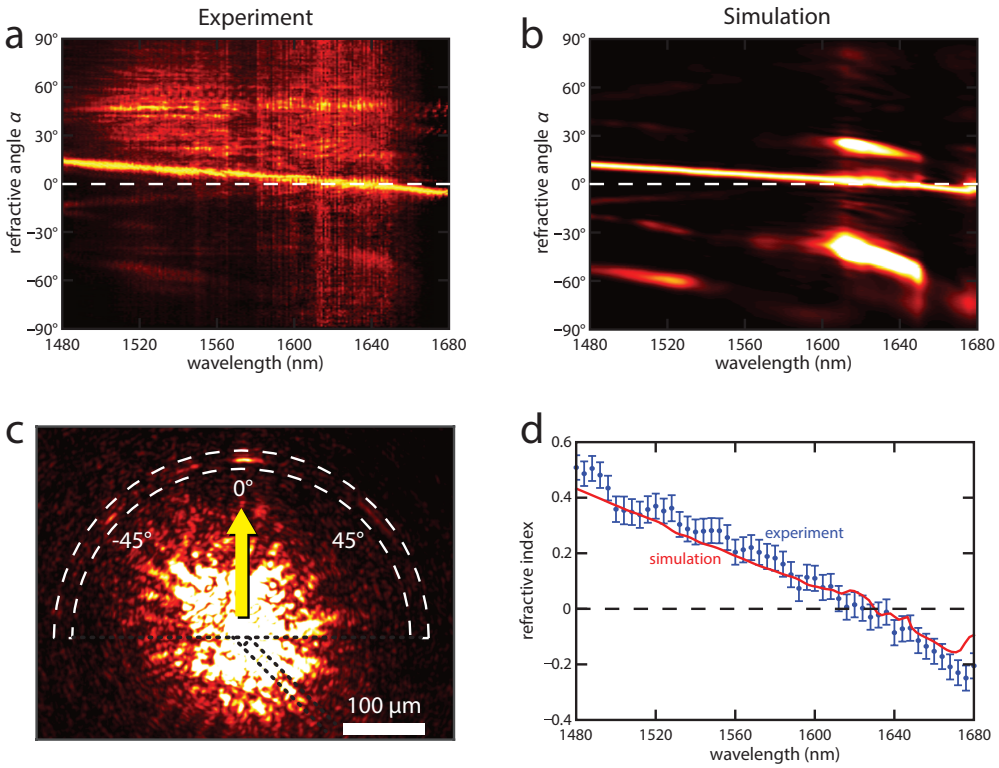

Fig. 4. Experimental refractive index measurement. (a) Measured near-field pattern and (b) corresponding simulated far-field pattern. The white dashed lines show that the refracted beam crosses 0° at a wavelength of 1625 nm. The image is normalized to the maximum intensity at each wavelength. (c) Near-infrared microscope image of the prism [Fig. 3] at 1625 nm, showing the refracted beam, which propagates normal to the interface between the prism and the SU-8 slab waveguide. The black dotted lines indicate the position of the prism and input waveguide. The white dashed lines delineate the portion of the image that is used to produce the measured near-field pattern [Fig. 4(a)]. (d) Effective index of the metamaterial extracted from the measured (blue dots) and simulated (red line) angles of refraction, α.

are unable to completely eliminate TM polarized light from the input source; as further proof, we observe modulation of this additional beam intensity while adjusting the polarization. A portion of this additional beam may be produced by light directly emitted from the input waveguide that has not successfully coupled to the metamaterial prism. We also simulated the refraction through a prism with the parameters matching that of the fabricated prism. The fabricated pitch and radius are found to be 720 nm and 193 nm, respectively, as measured by scanning electron microscope. As Fig. 4(b) shows, the experimental results are in excellent agreement with the simulation and the two exhibit the same zero-crossing wavelength [Fig. 4(b)]. The additional lobes in the simulated FFP at approximately +20° and -45° for wavelengths near 1625 nm are produced as an artifact of the finite simulation region (See Appendix A1 for simulation methods).

Fig. 4(c) shows a representative image of the refraction through the prism at a wavelength of 1625 nm, including the scattering from the edge of the slab waveguide. The refracted beam is observed directly above the prism, indicating refraction normal to the output facet and an effective index of zero. This shift in zero-index wavelength from the design target of 1550 nm can be attributed to fabrication imperfections.

Optics EXPRESS

We can extract the effective refractive index n_r^{eff} of the metamaterial prism from Snell's law,

$$n_{SU8}/n_r^{eff} = \sin 45^\circ / \sin \alpha, \tag{1}$$

where the angle of incidence on the output facet of the prism has been taken to be 45°, $n_{SU8} = 1.58$ (the mode index of the output polymer slab waveguide) and α is the measured angle of the scattered beam [Fig. 3(b)]. Figure 4(d) shows the index of refraction obtained from both the measurements and the simulation over the wavelength range from 1480 nm to 1680 nm. The extracted index ranges from 0.51 ± 0.04 at 1480 nm to -0.21 ± 0.05 at 1680 nm. The error bars in the experimental data are due to finite image resolution and fitting uncertainty. The fitting procedure is described in detail in previous work [33]. The relationship between index and wavelength is linear along the entire measurement range from 1480 nm through 1680 nm and in the vicinity of the zero-index wavelength of 1625 nm.

4. Robustness of modal degeneracy against fabrication imperfections

To consider the robustness of the modal degeneracy at the Γ point against fabrication imperfections, we simulate prisms with larger and smaller air-hole radii. Within a range of 0.8% of the target radii and 0.3% of the target pitch we find that the degeneracy and resulting zero-index is maintained with a wavelength redshift or blueshift. Most importantly, slight fabrication imperfections still produce the desired modal degeneracy and resultant zero-index behavior. At larger deviations from the ideal design, however, we observe the formation of photonic bandgaps. The appearance of these bandgaps is a further indication that the experimentally observed linear-dispersion behavior near the zero-crossing corresponds to the Dirac-cone-like dispersion (See Appendix A2 for an examination of the tolerance to fabrication imperfections).

5. Conclusion

We present the first CMOS-compatible zero-index metamaterial in the optical regime, featuring monolithic fabrication on an industry-standard 220-nm-thick SOI wafer. By eliminating metallic inclusions and high-aspect-ratio structures, this zero-index platform offers a significantly simplified fabrication procedure over earlier designs and compatibility with silicon foundries. In addition, satisfaction of homogenization criterion for in-plane normal incident light permits treatment of the platform as a metamaterial. As such, this metamaterial can be used for several zero-index applications, including supercoupling [19, 20], phase matching in nonlinear optics [30], and beam steering [26]. This design methodology can be extended to achieve a refractive index of zero using even thinner SOI layers and different material systems. In addition, this is the first experimental demonstration of an exceptional-ring-based zero-index metamaterial formed by the degeneracy of dipole and quadrupole modes. Integration with current silicon photonic platforms through monolithic fabrication and impedance matching offers a powerful platform for exploring the applications of zero-index materials.

Appendix

6. Methods

6.1. Simulation

The complex indices of silicon and silica for use in all numerical simulations were measured using spectroscopic ellipsometry. The complex effective constitutive parameters, and the far-field patterns were calculated using a commercial three-dimensional finite-difference time-domain solver. Reflected and transmitted electric fields were extracted at one point before the source and one after the metamaterial, respectively, to obtain the complex reflection and transmission

Optics EXPRESS

coefficients. The electric fields were collected from a near-field simulation to obtain the far-field pattern using far-field projection.

The band structures, electromagnetic mode profiles, dispersion surfaces and isofrequency contours were computed using a commercial three-dimensional finite element method solver. These results were obtained by calculating all the modes in a unit cell of the metamaterial with Floquet periodic boundary conditions in the x and y directions and perfectly matched layers at the boundaries in the z direction (i.e., out of the plane). TE-polarized modes were selected by evaluating the energy ratio of the magnetic fields in the x, y and z directions. Modes with low quality factors (<20) and confinement (<40%) were filtered out.

Modeling the full experimental device size (225 μm by 225 μm) [Fig. 3(a)] was extremely computationally intensive and we have limited our simulation region to 31.68 μm by 31.68 μm which results in a much shorter propagation region. This limited simulation region appears to be the source of additional beams observed in Fig. 4(b).

Further simulation methods are detailed in our previous work [33].

6.2. Fabrication

The metamaterial is fabricated using an SOI wafer with a 220-nm-thick silicon top layer. First, the air-hole array, input silicon waveguides, and silicon lip that is beneath the outside edge of the SU-8 slab waveguide are patterned via electron-beam lithography (EBL) into negative-tone resist (XR-1541 6%, Dow Corning). Reactive ion etching in an SF_6 : C_4F_8 atmosphere is then used to remove the silicon in the air holes and silicon surrounding the waveguides as shown in Fig. 1. The remaining negative-tone resist is then removed using 7:1 Buffered Oxide Etch (BOE). A 1.5-μm-thick SU-8 layer is spin-coated and patterned using EBL to form the output slab waveguide, then cured. Finally, a 2-μm-thick SU-8 waveguide is fabricated using the same method to form the calibration waveguide used to align images taken with the near infrared camera.

6.3. Parameter retrieval

We extract the reflected and transmitted electric fields at a point before the source and a point after the metamaterial, respectively, to obtain the complex reflection and transmission coefficients. Based on the complex reflection and transmission coefficients, we retrieve the complex constitutive parameters of the metamaterial using the retrieval method as described in reference [45].

6.4. Alignment of device

The additional polymer waveguide external to the polymer slab waveguide shown in Fig. 3(a) contains defects at ±45° and ±90° for a total of four alignment points. Scattering from these defects is imaged via an infrared camera and used to calibrate the angle of all experimental images.

7. Propagation loss

To estimate the propagation loss quantitatively, we perform a virtual cut-back measurement. Using finite-difference time-domain methods, we perform multiple simulations of wave propagation through 3 to 9 unit cells of the zero-index metamaterial. We excite the fundamental TE polarized mode into a silicon slab and monitor the power transmission into the identical fundamental mode in an identical silicon slab after the metamaterial. The transmission for various propagation lengths is fit to a linear regression, and we obtain a propagation loss of 1.12 dB/μm as shown in Fig. 5.

Optics EXPRESS

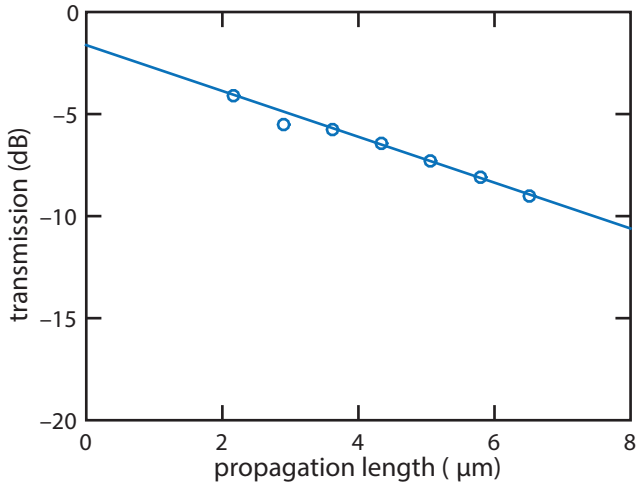

Fig. 5. The extracted transmission into the fundamental TE mode of the output slab as a function of propagation length within the ZIM. We fit to this transmission to a line and obtain a propagation loss of 1.12 dB/μm.

8. Tolerance to fabrication imperfections

We study the fabrication tolerance of the metamaterial design by examining the dependence of modal eigenfrequencies as a function of the hole radius and pitch [Fig. 1(d)]. We calculate the modes at the center of the Brillouin zone for pitches and radii that vary by ± 5% from the optimal device parameters, with pitches ranging from a = 695 nm to a = 765 nm and for hole radii r = 210 nm to r = 235 nm. We distinguish the quadrupole mode from the dipole modes by their disparate quality factors, which is significantly higher in the quadrupole modes.

In Fig. 6(a), we plot the average eigenfrequency of the quadrupole and dipole modes at the Γ point as a function of the lattice parameters. The white dashed line indicates the dimensions for which the average eigenfrequency of the two modes is equal to the operation wavelength, λ = 1550 nm. We calculate the band structure at multiple points [Fig. 6 I, II, III, and IV] along this line. For dimensions that are larger or smaller than the optimal design, the quadrupole and dipole modes are non-degenerate; for smaller radius and pitch values, the dipole mode has a higher eigenfrequency than the quadrupole mode. As we increase the dimensions along the white dashed line, the gap between the higher-frequency dipole modes and the lower-frequency quadrupole mode decreases until we reach an optimal structure with perfect modal degeneracy (indicated in Fig. 6(a) by the red star and corresponding to our ideal design parameters). For even larger dimensions along the white dashed line, the gap once again increases; however the position of the modes is reversed with respect to the operating frequency, as the dipole modes have lower frequency than the quadrupole mode (Fig. 6 I and II, versus Fig. 6 III and IV).

The absolute difference between the modal eigenfrequencies for the same range of geometries is shown in Fig. 6(b). The dark blue region corresponds to a degeneracy of the two modes (0 nm difference between the two eigenfrequencies). The red circle in Fig. 6(b) indicates the single parameter configuration that corresponds to the degeneracy of the two modes at the operation wavelength, λ = 1550 nm. If we allow a small wavelength bandgap of 1 nm to form between the modes, we can tolerate a fabrication variance of ± 0.3% (≈ 2 nm) in the pitch and an imperfection of ± 0.8% (≈ 2 nm) in the hole radii while still maintaining near degeneracy at the operation wavelength.

Optics EXPRESS

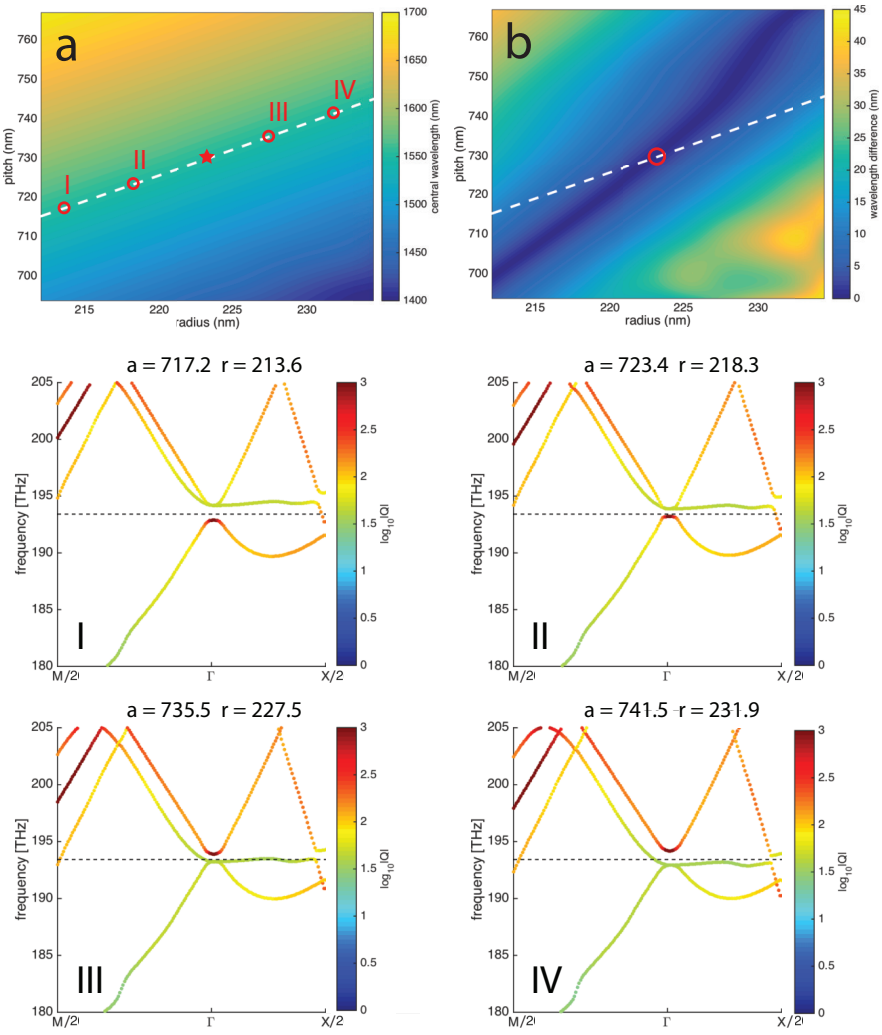

Fig. 6. (a) The average eigenfrequency as a function of the lattice parameters. The white dashed line indicates the range of values where the average eigenfrequency of the modes occur at the operation wavelength (λ= 1550 nm). The red circles indicate points where sample band structures are calculated (as shown in I, II, III, and IV). The red star indicates the point with the ideal pitch and radius [Fig. 2(a)] to achieve degeneracy of the modes at the operation wavelength. (b) The absolute difference between the modal eigenfrequencies as a function of lattice parameters. The dashed white line indicates the range of values where the average eigenfrequency of the modes is equal to the operation wavelength [from Fig. 6(a)]. The dark blue region corresponds to a degeneracy of the two modes (0 nm difference between the two eigenfrequencies). The red circle indicates the single parameter configuration that corresponds to the degeneracy of the two modes at the given operation wavelength.

9. Homogenization

We conduct a systematic analysis of the on-chip Dirac-cone metamaterial to verify that it can be treated as a homogeneous effective medium with respect to in-plane propagating waves. In this analysis, we consider the homogenization criteria and locality conditions. Since our structure [Fig.

Optics EXPRESS

1(d)] is only periodic in the in-plane direction, this analysis is restricted to in-plane propagation. In this paper, we assume harmonic time dependence of $e^{-i\omega t}$.

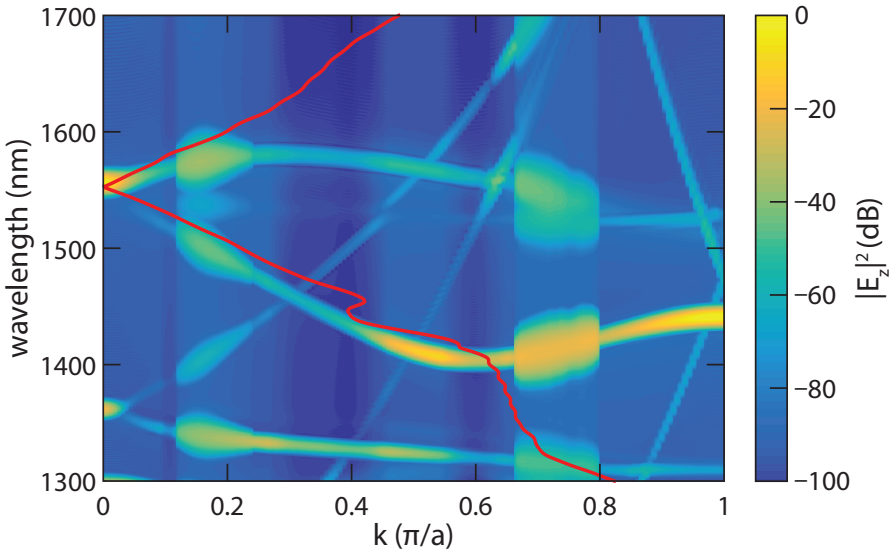

Fig. 7. Comparison of band structures of the presented metamaterial [Fig. 1(d)] computed by determining the angular frequencies as a function of wave vector for all the Bloch modes (color map), and by $k = n_r^{\text{eff}}\omega/c$ with the retrieved effective index n_r^{eff} (red line).

9.1. Homogenization criteria

The general homogenization criterion of metamaterials requires that $k_0 a, ka \leq 1$ where a is the lattice constant or period [Fig. 1(d)], k_0 is the free-space wavenumber, and k is the effective wavenumber in the metamaterial [46]. These criteria ensure that we can avoid the unwanted diffraction of waves within the metamaterial, because the effective wavelength is much larger than the lattice constant. Similarly, we also avoid diffraction of waves at the boundary, since the lattice constant is smaller than the free-space wavelength. We can evaluate the homogenization criteria by studying the photonic band structure of the metamaterial, which is treated as an infinite array. Since the Dirac cone appears near the Γ point [Fig. 2(a)] where the effective wavenumber k approaches zero, this metamaterial meets the criterion $ka \leq 1$ in the vicinity of the Dirac point. To quantitatively estimate the region of the band structure in which the effective medium model is valid, we compare band structures obtained using two different methods: a macroscopic method that treats the metamaterial as a homogeneous medium (using the retrieved effective index n_r^{eff} and the expression $k = n_r^{\text{eff}}\omega/c$), and a microscopic method that calculates the Bloch wavevectors of eigenmodes of the metamaterial [Fig. 7]. For propagation along the Γ-X direction, the two band structures agree well in the range $0 < k < 0.6$ at wavelengths below the Dirac point, and $0 < k < 0.2$ at wavelengths above the Dirac point. The effective medium model follows the linear band of the Dirac-like cone even where it crosses with another band near $k \approx 0.3$ and $\lambda = 1470$ nm. Thus, it is reasonable to treat the infinite array as a homogeneous medium with effective constitutive parameters within these regions.

The Dirac-like cone is composed of three bands, which become degenerate near the center of the Brillouin zone, forming a ring of exceptional points [39]. Within the ring, the degenerate bands can be decomposed into a quadrupole and two dipole modes. Outside of the ring, at larger in-plane wavevectors, the degeneracy is broken: the bands with linear dispersion [Fig. 2(a)] are

Optics EXPRESS

instead described by linear combinations of the quadrupole and transverse dipole modes, which oscillate in quadrature [Visualization 1-Visualization 2]. Here we show the vertical component of the magnetic field, H_z, with a wavevector at the boundary of the exceptional ring. These hybridized modes form a conjugate pair, resulting in positive and negative phase velocity for the high and low frequency branch, respectively. Each mode has a positive group velocity, as indicated by the black arrow in the animations. The remaining longitudinal dipole forms the flat band [Visualization 3], and is not excited by plane waves due to symmetry mismatch. Therefore, incident plane waves excite the linear dispersion bands, resulting in a positive- or negative-index propagation for high or low frequencies, respectively. In both cases, the effective index approaches zero for frequencies near the Dirac point. As a result, the metamaterial can be treated as an effective medium with an effective index near zero and linear dispersion. These phenomena are isotropic, as we observe a similar modal decomposition in the metamaterial for waves propagating along the Γ-M direction [Visualization 4, Visualization 5, and Visualization 6].

To further investigate the homogenization at the boundary, we simulate the angle-dependent transmission of our Dirac-cone metamaterial [Fig. 8]. We expect transmission at only normal incidence since obliquely incident waves will be perfectly reflected from a index-near-zero medium due to total internal reflection. As shown in Fig. 8(a), we calculate the transmission through a metamaterial slab with a thickness of five unit cells along the propagation direction. Fig. 8(b) shows the transmission spectrum at incident angles ranging from 0° (normal incidence) to 80°, in the plane of the array.

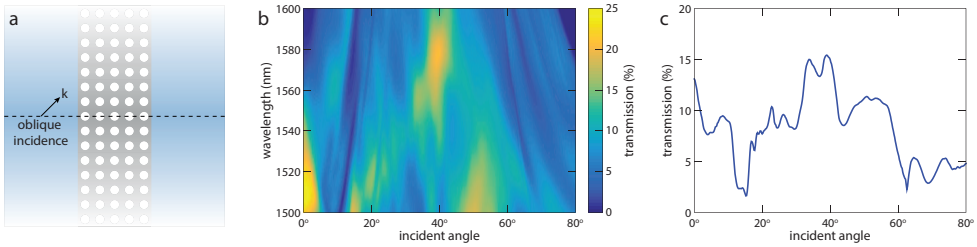

Fig. 8. Dirac-cone metamaterial with oblique incidence. (a) Top-down view of the Dirac-cone metamaterial. (b) Angle-dependent transmission of the Dirac-cone metamaterial. (c) Angle-dependent transmission at the design wavelength of 1550 nm

We observe high transmission near normal incidence in the wavelengths from 1500 to approximately 1560 nm, indicating strong angular selectivity as a result of the near-zero effective index in this regime [Fig. 2(d)]. In the regime where the wavelength is longer than ~1570 nm, transmission at normal incidence decreases significantly due to a partial bandgap along the Γ-X direction [Fig. 7].

In addition, extraneous transmission at higher angles of incidence can be attributed to incident light coupling into additional modes at large k values in the band structure [Fig. 7]. We can more closely observe the extraneous transmission at the design wavelength in Fig. 8(c). Notably, we observe an additional transmission peak at around 20 to 60° incidence. At these incidences, we believe it is plausible that there is coupling into the flat band and additional bands which are not selective to only normal incidence light (See Appendix A4.3).

9.2. *Locality conditions*

We expect the effective constitutive parameters of metamaterials to satisfy the conditions of locality: passivity, causality, isotropy, and absence of radiation loss [44]. Fig. 9(b) shows that the medium is passive, since $\mathbf{Im}(\epsilon_r^{\text{eff}}) > 0$ and $\mathbf{Im}(\mu_r^{\text{eff}}) > 0$ simultaneously near the Dirac-point wavelength. As shown in Fig. 9(a), both $\delta(\mathbf{Re}(\epsilon_r^{\text{eff}}))/\delta\omega < 0$ and $\delta(\mathbf{Re}(\mu_r^{\text{eff}}))/\delta\omega < 0$ near the

Optics EXPRESS

Dirac-point wavelength, indicating that the medium satisfies the basic causality conditions represented by the Kramers-Kronig relations [47]. The retrieved ϵ_r^{eff} and μ_r^{eff} show anomalous dispersion at wavelengths larger than 1570 nm due to a partial bandgap in this wavelength regime [Fig. 7].

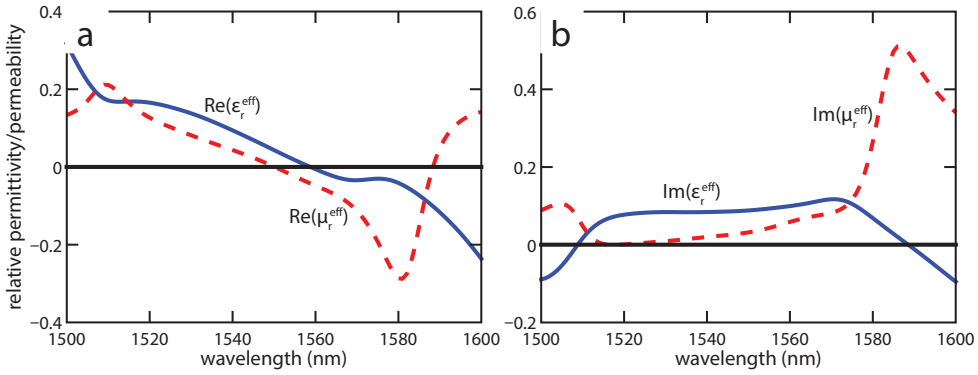

Fig. 9. (a) Real and (b) imaginary parts of the effective relative permittivity and permeability of the metamaterial retrieved from numerically calculated reflection and transmission coefficients.

To analyze the isotropy of our Dirac-cone metamaterial, we compute the isowavelength contours of the modes forming the Dirac cone near the Dirac-point frequency. The degree of isotropy of a mode at a given frequency can be evaluated by the shape of its isowavelength contour [36]; a perfectly circular isowavelength contour indicates isotropic behavior. We can quantitatively estimate how circular an isowavelength contour is by fitting it to a "super-circle" relation, which obeys the equation $x^n + y^n = r^n$. This relation describes a perfect circle when $n = 2$ and a square with a side length of $2r$ as $n \to \infty$ where n is defined as the order of the super-circle.

As the operating wavelength strays from the Dirac-point frequency, the fit of the isowavelength contours to supercircles gradually increases in order, as shown in Fig. 2(e). We fit each contour to a supercircle, and plot the extracted radii r and supercircle orders n along with the 95% confidence intervals extracted from the fits in Fig. 10. The super-circle order indicates whether the modes are isotropic (circular) around the Γ point. Fig. 10(a) shows that the structure behaves like an isotropic medium for the frequencies between $f \approx$192–195 THz, where the approximate order of the fitted supercircles is equal that of a perfect circle ($n = 2$). This corresponds to an operating bandwidth of $\Delta\lambda = 20$ nm centered at $\lambda = 1550$ nm.

In our previous work [33], the bands were strictly conical, with linear dispersion. In comparison, the bands in this work are more quadratic due to the asymmetry in the quality factor of the modes. The quality factor of the pillar structure's monopole and dipole modes are approximately 105 and 50 (in comparison, the air hole dipole and quadrupole modes quality factors are estimated to be 40 and 5500). The greater asymmetry in quality factors results in the quadratic dispersion observed [Fig. 2(a)]. This is manifested as a smaller isotropic bandwidth around the zero-index wavelength.

In Fig. 10(b), the extracted supercircle radii first decrease and then increase as a function of frequency, both with a strongly linear trend ($R^2 > 0.99$). This linear behavior strengthens the claim that the metamaterial possess a linear dispersion corresponding to a Dirac cone.

Optics EXPRESS

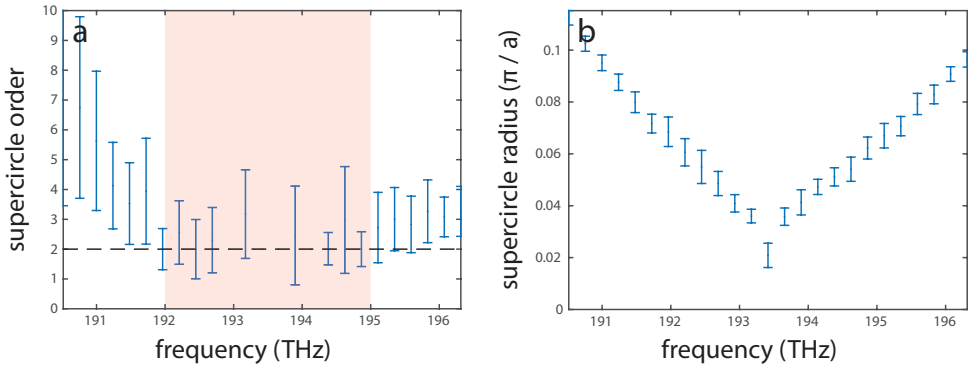

Fig. 10. (a) The range of super-circle order as a function of frequencies, where $n = 2$ corresponds to a perfect circle. The highlighted region ($f \approx$ 192–195 THz) exhibits approximately circular isofrequency contours. (b) The extracted supercircle radii showing that the radii decrease and then increase linearly as a function of frequency.

9.3. *Modal analysis*

To determine which modes can be accessed via normal incident TE plane wave excitation, we replot the bandstructure as shown in Fig. 2(a) such that the marker size corresponds to confinement in Fig. 11. If we consider only the Γ-X direction corresponding to normal incidence, we maintain that the presented structure can be homogenized as a bulk medium with effective constitutive parameters as modes beside those forming the Dirac cone fall under one of the following criteria: 1) the band has a weak TE characteristic and is unlikely to be excited by a TE source, 2) the band corresponds to a mode that is incompatible with a plane wave due to its symmetry and is unlikely to be excited by a plane-wave source.

With this in mind, we can characterize the relevant bands as follows:

Mode 1: The mode denoted corresponds to the photonic band leading into the Dirac cone. At the zero-index wavelength and at the Γ point we observe the two modes forming the zero index: the electric dipole mode and magnetic quadrupole mode, degenerating at the center of the Brillouin zone. These modes have a strong TE characteristic and are compatible with plane-wave symmetry [Fig. 2(c)]; as such, they meet both criteria and are most likely to be excited.

Mode 2: This mode corresponds to a "flat" band at the Γ point. The flat band cannot be excited under the TE-polarized incident light due to the fact that the flat band corresponds to a electric longitudinal dipole mode, which is orthogonal to the electric field of the TE-polarized incident light. Although this band fulfills the first criterion, it fails the second and is unlikely to be excited.

Modes 3, 4 and 5: Traveling along the Γ-X direction, we observe another band around $k = 0.75$X (between modes 4 and 5, curving upward). We begin observing longitudinal characteristic in the modes at around mode 3. This longitudinal characteristic becomes more prevalent as we follow the band toward modes 4 and 5, similar to the longitudinal characteristic observed in the flat band. This indicates increasing symmetry mismatch with a plane wave source; for example, we observe two nodes on the edges of the mode corresponding to mode 4. The modes corresponding to the denoted points are shown in animations: Visualization 7, Visualization 8, Visualization 9, Visualization 10, Visualization 11, Visualization 12, Visualization 13, Visualization 14, Visualization 15, and Visualization 16.

We find that only the modes at the zero-index wavelength and Γ point fulfill both criteria and expect that this hybrid mode is the only mode accessed at normal incidence. As a result, it is reasonable to treat this structure as a bulk medium with effective constitutive parameters around the Dirac-point frequency.

Optics EXPRESS

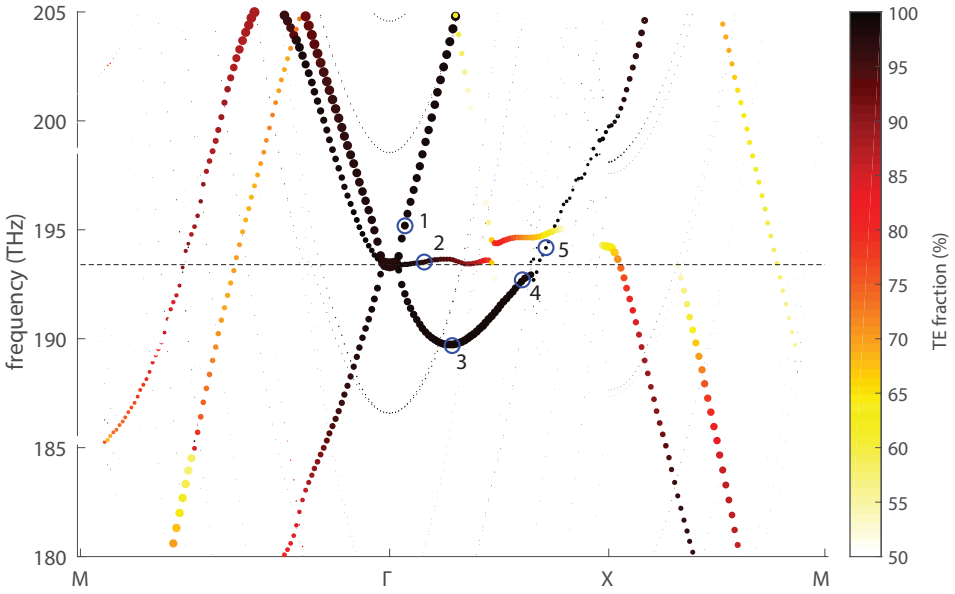

Fig. 11. Photonic band structure of the zero-index metamaterial for TE modes with marker size corresponding to confinement (larger circles correspond to higher confinement and smaller circles correspond to lower confinement) and TE fraction superimposed.

10. Power flow

To verify that the hybrid zero-index mode of our metamaterial can support a traveling wave with real power flow, we conduct a finite-difference time-domain simulation with a pulse source for a finite slab of ten unit cells in the propagation direction and periodic boundary conditions in the perpendicular orientation [Fig. 12(a)].

As shown in this simulation, we observe energy enter the metamaterial region (denoted as the area between the two dotted lines) at around 400 fs at a group velocity of v_1, propagate through the metamaterial at a different group velocity of v_2, and exit at around 800 fs at the original group velocity of v_1 [Fig. 12(b)]. This simulation shows our metamaterial supporting the propagation of a traveling wave with real power flow from left to right [Visualization 17].

The power flow Poynting vector field for the mode at the Γ point, which clearly indicates real power transfer from right to left [Visualization 18].

Author contributions

Y.L. conceived the basic idea for this work. Y.L., O.R., P.M., and D.V. carried out the FDTD simulations. O.R., S.K., P.M., and M.Y. carried out the FEM simulations. O.R. and D.V. designed the optical waveguides. D.V. performed the fabrication. O.R. and D.V. carried out the measurements. P.M. analyzed the experimental results. M.L. and E.M. supervised the research and the development of the manuscript. D.V. wrote the first draft of the manuscript, and all authors subsequently took part in the revision process and approved the final copy of the manuscript.

Optics EXPRESS

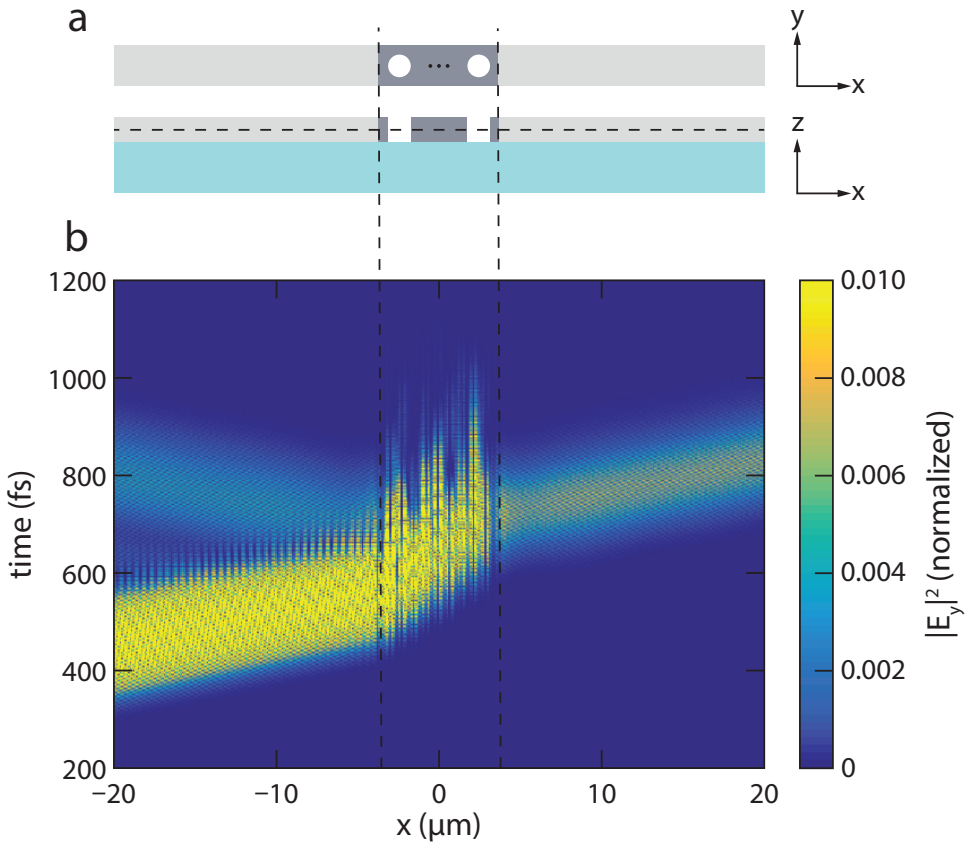

Fig. 12. Finite-difference time-domain simulation of the metamaterial with a pulse source. (a) Top: top-down view of the simulation region. The metamaterial includes 10 unit cells. The vertical dashed lines indicate the boundaries of the metamaterial. Bottom: cross-section view of the simulation region, in which the horizontal dashed line indicates the position of the monitor planes. (b) Electric field intensity at different positions in the simulation region over the duration of the simulation.

Funding

National Science Foundation (DMR-1360889); the Air Force Office of Scientific Research (FA9550-14-1-0389); National Science Foundation Graduate Research Fellowship Program; the National Department Science and Engineering Graduate Fellowship (from AFOSR); Natural Sciences and Engineering Research Council of Canada Postgraduate Doctoral Scholarship.

Acknowledgments

The authors thank Chua Song Liang, Zin Lin, Olivia Mello, Cleaven Chia, Haoning Tang, Dario Rosenstock, Lysander Christakis, and Kevin Lee for helpful discussions and assistance with simulations, as well as Nabiha Saklayen and Reza Sanatinia for feedback on the manuscript throughout its development. This work was performed in part at the Center for Nanoscale Systems (CNS), a member of the National Nanotechnology Coordinated Infrastructure Network (NNCI), which is supported by the National Science Foundation (1541959). CNS is part of Harvard University.